Nondestructive Characterization of Magnetic Polymeric Scaffolds Using Terahertz Time-of-Flight Imaging

Sonia Zappia, Rosa Scapaticci, *Member, IEEE*, Matteo Bruno Lodi, *Member, IEEE*, Alessandro Fanti, *Senior Member, IEEE*, Giuseppe Ruello, *Senior Member, IEEE*, Lorenzo Crocco, *Senior Member, IEEE*, and Ilaria Catapano, *Member, IEEE*

***Abstract*—Magnetic scaffolds (MagS) are 3-D composite materials, in which magnetic nanoparticles (MNPs) are used to load a polymeric matrix. Due to their wide use in several medical applications, there is an increasing demand of advanced techniques for nondestructive quality assessment procedures aimed at verifying the absence of defects and, more generally, dedicated to the characterization of MagS. In this framework, the use of terahertz (THz) waves for nondestructive characterization of multifunctional scaffolds represents an open challenge for the scientific community. This article deals with an approach for the characterization of MagS by means of a THz time-domain system used in reflection mode. THz analyzes are performed on poly-caprolactone (PCL) scaffolds magnetized with iron oxide (Fe_3O_4) MNPs through a drop-casting deposition and tuned to obtain different distributions of MNP in the biomaterial. The proposed data processing approach allows a quantitative characterization of the MagS, in terms of their (estimated) thickness and refractive index. Moreover, the proposed procedure allows us to identify the areas of the scaffold wherein MNP are mainly concentrated, and thus, it gives us information about MNP spatial distribution.**

***Index Terms*—Composite materials, magnetic nanoparticles (MNPs), nondestructive inspection, terahertz (THz) imaging.**

I. Introduction

COMPOSITE materials are a combination of two or more materials that differ in terms of chemical or physical properties and are merged to create a new material having a separate and distinct final structure [1], [2], [3], [4]. Polymer-based composite materials have emerged as an interesting alternative to other materials (i.e., metals, plastics, and ceramics) in several applications, thanks to their mechanical properties, flexibility, and structural integrity [5]. However, it is worth noting that the physical and chemical manufacturing routes of composite materials are complex [6], [7], [8]. In this regard, it is ever-increasing the demand for effective, possibly nondestructive procedures for quality assessment [5]. Among composite materials, magnetic polymer-based scaffolds raised a huge interest due to their wide use in several medical applications, such as cancer therapy [9], tissue engineering [10], and drug delivery [11]. A magnetic scaffold (MagS) can be obtained by physical loading of magnetic nanoparticles (MNPs) into a polymeric matrix to obtain a multifunctional and theranostic device [12], [13], [14]. The advantage of MagS is that they can be controlled using an external magnetic field, which makes them appealing for applications in which the scaffold must be implanted in vivo, such as tissue repair [15]. Furthermore, MagS can target and control the delivery of soluble factors, such as growth factors, hormones, and peptides directly to the implantation site under the magnetic field to improve the fixation and stability of implant [16] and has good mechanical properties [17] and excellent biocompatibility [18]. However the production process of MagS is often associated to a nonuniform final spatial distribution of MNPs in the polymeric matrix [19], so that recent and intense progresses on the manufacturing strategies are ongoing. The potential of MagS and the need to control the quality of their productive process motivate the development of procedures for routine and reproducible nondestructive characterization of MNP distribution in the polymeric matrix.

Currently, several methods are exploited to analyze MagS, such as microcomputed tomography (MicroCTs) [20], [21], scanning electron microscope (SEM) [22], [23], [24], and transmission electron microscopy (TEM) [22], [25], [26] and each one of them has its advantages and drawbacks.

MicroCT uses X-rays to capture the image and, hence, shape and size of the polymer and nanocomposite fibers [20], [21]. The images obtained through the Micro-CT system scan allows for the 3-D reconstruction of the nanocomposite fibers and, hence, the distribution of MNPs along the fibers [20]. X-rays systems provide high resolution images but have the disadvantage of using ionizing radiations, always related to risks involving the operator, as well as the material itself that could be damaged [27].

Manuscript received 6 October 2022; revised 24 March 2023; accepted 4 May 2023. Date of publication 11 May 2023; date of current version 3 July 2023. This work was supported by PRIN BEST-Food-Broadband Electromagnetic Sensing Technologies for Food quality and security assessment-B64I19001250001. *(Corresponding author: Ilaria Catapano.)*

Sonia Zappia, Rosa Scapaticci, Lorenzo Crocco, and Ilaria Catapano are with the Institute for Electromagnetic Sensing of the Environment, National Research Council of Italy, 80124 Naples, Italy (e-mail: zappia.s@irea.cnr.it; scapaticci.r@irea.cnr.it; crocco.l@irea.cnr.it; ilaria.catapano@cnr.it).

Matteo Bruno Lodi and Alessandro Fanti are with the Department of Electrical and Electronic Engineering, University of Cagliari, 09123 Cagliari, Italy (e-mail: matteob.lodi@unica.it; alessandro.fanti@diee.unica.it).

Giuseppe Ruello is with the Department of Electrical Engineering and Information Technology University of Naples "Federico II," 80125 Naples, Italy (e-mail: giuseppe.ruello@unina.it).

Color versions of one or more figures in this article are available at https://doi.org/10.1109/TTHZ.2023.3275286.

Digital Object Identifier 10.1109/TTHZ.2023.3275286

SEM uses a focused beam of high-energy electrons to generate a variety of signals at the surface of solid specimens. The signals derived from electron-sample interactions reveal information about the sample including surface morphology (texture). The shape and the porosity of MagS were observed by SEM images in several works available in the literature [22], [23], [24], [28]. However, SEMs are expensive and must be housed in an area free of any possible electric, magnetic, or vibration interference. Moreover, to investigate the sample in depth, slicing and destructive preparation are needed [29].

TEM is a microscopy technique in which a beam of electrons is transmitted through the sample under test to form an image. The image is derived from the interaction of the electrons with the sample as the beam is transmitted through it. TEMs provide topographical, morphological, compositional, and crystalline information. The images allow researchers to view samples at a molecular level, making it possible to analyze structure and texture [30]. This type of technique has been used to explore the morphology of the MNPs distributed along the fibers of the scaffolds [22], [25], [26]. However, to obtain a TEM image, samples must be sliced thin enough for electrons to pass through (i.e., usually the specimens has an ultrathin section less than 100 nm). Therefore, nondestructive evaluation is not possible. Moreover, the specimens must be prepared as a thin foil, or etched to be thin enough for the beam to penetrate. Constraints make the sample preparation laborious. Furthermore, other disadvantages are that TEM systems are large and very expensive and their operation and analysis requires special training [29].

Thanks to its unique properties, terahertz (THz) imaging may represent a potential candidate for MagS nondestructive characterization. THz are electromagnetic (EM) waves ranging from 0.1 to 10 THz (wavelength from 3 mm to 30 μm), which are able to penetrate a wide range of nonconducting materials, e.g., plastics, polymers, ceramics, wood, and glass [31], just to name a few. THz waves are nonionizing, thus allowing nondestructive inspection of the materials without requiring specific security protocols. Various applications of THz waves have been reported in many fields, including medical diagnosis [32], pharmaceutical analysis [33], security enhancement [34], cultural heritage [35], and food quality control [36]. However, THz waves are strongly attenuated by water and suffer from the environmental conditions, such as humidity [37].

One of the most promising applications of THz technologies [38] is the nondestructive evaluation of composite materials [37], [39], [40], [41], [42], [43], [44], [45], [46]. In particular, a number of efforts have been dedicated to nondestructive evaluation of polymeric (dielectric) scaffolds [47], [48], [49]. THz technology has been exploited for the detection of damages, such as nonimpregnated areas in polymer composite materials [37], [50], [51], or for the evaluation of the porosity of the polymeric matrix [5]. Considering the abovementioned framework, this article presents a method for the nondestructive characterization of MagS and the determination of the distribution of MNP in the polymer matrix, using THz technology. It is worth noting that although THz technology is well known for the nondestructive testing of composite materials, to the best of the authors' knowledge, its application to MagS is a new challenge that has not yet been thoroughly investigated by the scientific community. This article describes the procedure used in [52], [53], and [54], where THz imaging was applied to MagS for the first time. A measurement protocol is developed for the quantitative characterization of MagS, allowing estimation of thickness (Δ) and refractive index (η). The 2-D distribution of MNPs in the MagS is determined using an ad hoc procedure based on the analysis of THz data collected during the experiments and the use of reference time-of-flight (ToF) values calculated considering homogeneous ideal scaffolds. In order to characterize the spatial distribution of the MNPs two indices are introduced: 1) the magnetization index (I_m), which accounts for the amount of MNP in the scaffolds; 2) the magnetization distribution index (I_{md}), which takes into account the areas where MNP are more concentrated (with respect to a homogeneous distribution of MNP in the scaffold). 2-D maps are presented to visually detect the presence of MNP in MagS and to identify the areas where MNP are most concentrated and their distribution in the polymer matrix.

The rest of this article is organized as follows. Section II introduces the general concept of MagS with a specific focus on our case studies, Section III describes the ToF sensing principle, the measurement system, the data filtering used, and the measurement protocol applied to the laboratory case studies. Section IV is devoted to describe the strategy adopted to determine the thickness, the refractive index, and the MNPs spatial distribution of MagS. In Section V, the results are presented. The discussion follows in Section VI. Finally, Section VII concludes this article.

II. Materials

A. Magnetic Scaffolds

MagS are 3-D composite materials, in which iron oxide (Fe_3O_4) MNPs are used to load a polymeric matrix made of poly-caprolactone (PCL).

It is well known that polymer scaffolds used for tissue engineering should possess proper architecture and mechanical properties to support cell adhesion, proliferation, and differentiation [55]. Typical scaffold designs have included meshes and fibers; these designs are chosen because they promote uniform cell distribution, diffusion of nutrients, and the growth of organized cell communities [56]. Therefore, the architecture of a PCL scaffold is made using fibers that are superimposed on each other forming a grid to obtain a solid structure having a certain porosity. The choice of the ideal fiber size and the porosity of the scaffold depends on the proposed function of the scaffold itself [57].

Regarding the process of incorporation of MNP into the polymer matrix, the one used for the analyzed MagS consists of dropping the MNP dispersed in water onto the PCL scaffolds and the deposition occurs under the driving force of an external magnet [52].

B. Laboratory Case Studies

Polymeric scaffolds produced by 3-D Biotek (3-D Biotek LLC) have been considered in this study. The set of 3D-Insert are constituted by a 90°-interlaced fiber architecture, with a

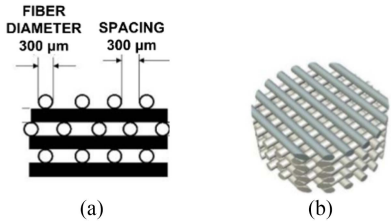

Fig. 1. (a) 3D-Insert consisting of a 90°-interlaced fiber architecture, with a fiber diameter of 300 μm, spaced by 300 μm. (b) Image of the 3-D structure of the scaffold.

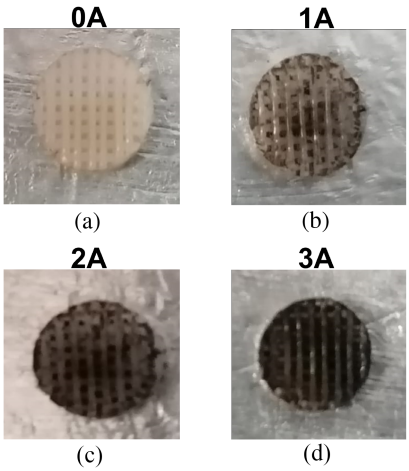

Fig. 2. Photos of the samples. (a) scaffold without MNPs named sample 0 A. (b)–(d) Scaffolds with a different amount of MNPs and referred as sample 1 A, 2 A, and 3 A, respectively.

fiber diameter of 300 μm, spaced by 300 μm, resulting in a nominal porosity of about 80% [see Fig. 1(a)]. These standard poly-caprolactone (PCL) disks have a 5 mm diameter. A representative image of the 3-D structure of the scaffold is shown in Fig. 1(b). The drop-casting deposition is tuned to obtain different distributions of MNPs in the biomaterial as described in [52]. The four MagS analyzed in this study are shown in Fig. 2, where the sample named 0 *A* does not contain MNPs and is used as reference.

III. Methods

A. Sensing Principle of the Measures

THz pulsed imaging, also known as THz ToF imaging, has the unique property of providing a 3-D map of the object under test by exploiting THz data collected in reflection mode [58]. This technique was used for the first time by Mittleman and coworkers to produce the internal structure of a 3.5 in floppy disk [59]. In brief, the object is probed by a pulsed signal and the reflected waveform is collected as a time-dependent function within a certain observation time window by using a THz time-domain system (TDS) configuration.

By plotting the gathered waveform referred to a measurement point, a trace showing the amplitude-time of the reflected signal over the target (called A-scan) is obtained, which accounts for the reflection from the object surface and its inner EM features

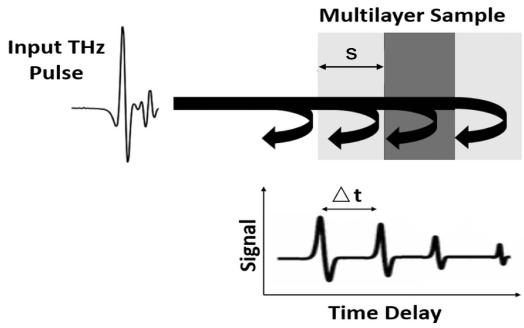

Fig. 3. ToF sensing principle: probing THz pulse (left upper panel); pulse interaction with a multilayer sample (right upper panel); collected THz signal due to the multilayer sample (lower panel).

(if the object is nonmetallic) [60] (see Fig. 3). The vertical axis of the A-scan represents the amplitude of the signal, the horizontal axis is the time axis and represents the ToF, that is, the time t that the waveform employs to propagate from the emitter to an EM discontinuity and to go back to the receiver. The ToF t is related to the distance d between THz probes and the detected discontinuities as

$$t = \frac{2\,d}{v}. \tag{1}$$

v being the EM wave propagation velocity into the object.

It is worth to pointing out that, starting from the measured signals, several THz images can be generated, each one revealing a different feature of the analyzed sample. For example, an image obtained by plotting the temporal position of the first peak of the gathered waveforms at each measurement point, reveals differences in the refractive index and the surface tomography of the sample [61]. Furthermore, by plotting, pixel by pixel, the signal amplitude occurring in a specific time window, a THz false color image is derived, which accounts for the inner features of the object.

The effectiveness of THz imaging and, more generally, of EM diagnostics benefits from a data processing tool aimed at improving the imaging performance of the hardware device. In fact, undesired signals, like noise and clutter, corrupt the useful data and, thus, the imaging capabilities. Therefore, data filtering procedures are useful to reduce noise and clutter and improve the imaging results.

B. Measurement System and Filtering Procedure

THz data have been collected by means of the fiber coupled THz time domain (FiCO), shown in Fig. 4. The system consists of the following three main components:

1) the FiCO base unit;
2) emitter and receiver heads;
3) the laser source.

The laser source is a free-space pulsed laser working at 1560 nm with average power higher than 200 mW and it acts as primary source. The laser signal is driven into FiCO base unit by means of two steering mirrors. The FiCO base unit splits the input signal into a pump and probe beam used to generate THz waves and it is connected the emitter and receiver heads

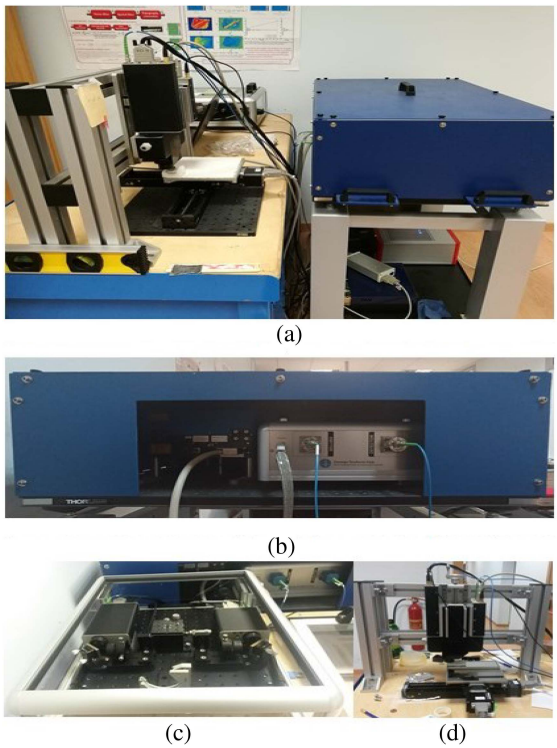

Fig. 4. Zomega Fico system. (a) Global view. (b) Primary laser source and optical delay line. (c) Purge chamber. (d) Imaging module.

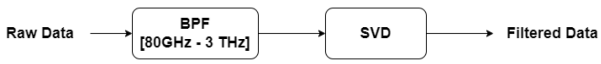

Fig. 5. Signal Filtering Procedure: Step 1-BPF; Step 2-Filtering procedure based on the data matrix SVD.

by means of fiber optic cables. The system collects data in the nominal frequency range from 80 GHz up to 3 THz (lower and higher frequency signal components are overlapped by noise) and the estimated THz beam size at the focal point is about 1 mm. The system is equipped with an ad hoc designed imaging module, which allows measurements in normal reflection mode. In particular, the object under test is positioned on a movable platform, which automatically scans a 150 mm $\times$ 150 mm maximum area with a minimum spatial offset of 0.12 mm, and it is located at the focal distance by manually adjusting the height of the THz normal reflection module. 3-D data (2-D in space + 1-D in time) are collected within a 100 ps observation time window. The waveform acquisition speed can be up to 500 Hz, and the maximum dynamic range (DNR) is 30 dB, while the typical DNR is 20 dB. The data can be visualized and processed after the measurement stage.

Concerning data processing, an ad hoc strategy has been designed in order to filter data and visualize THz images. This strategy involves two different steps in time-domain aimed at reducing noise and filtering out undesired signal introduced by the adopted THz system, as shown in the flow chart in Fig. 5. The first step aims at removing the undesired low and high-frequency signal components and it is made up of a frequency band-pass

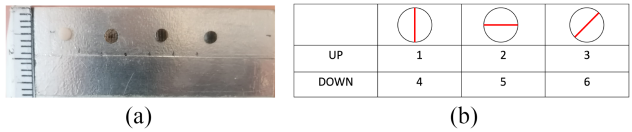

Fig. 6. (a) Samples placed on a metal plate. (b) Measurement set up; we will refer to the six configurations with numbers from 1 to 6.

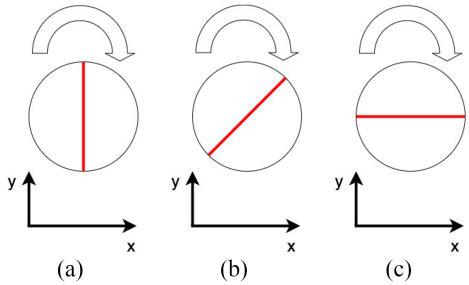

Fig. 7. Different fibers orientations used to carry out the measurement. (a) Starting position $\alpha = 0°$. (b) Rotaded by $45°$. (c) Rotaded by $90°$.

filter (BPF) procedure selecting the signal components in the range 80 GHz–3 THz. The second step is a noise filtering procedure based on the singular value decomposition (SVD) of the band pass filtered data matrix. The SVD data filtering procedure, which is detailed in [35], filters the noise out, while preserves the image details, by using a suitable threshold T_{svd}. A good choice is to set T_{svd} in such way that the energy of the filtered data matrix is about the 90%–95% of the energy of the collected data matrix [62]. In the case of THz imaging, as shown in [35], it is observed that, the singular spectrum of a generic data matrix is characterized by a fast decay followed by a smooth (almost constant) behavior of the singular values. Accordingly, T_{svd} is chosen as the index of the singular value in correspondence of the point where the spectrum changes its slope, i.e., the index of the singular value where the fast decay of the singular values is followed by the smooth one.

C. Measurement Protocol

The procedure used to carry out the measurements of the samples under test (SuT) can be summarized in the following step.

1) The samples are placed on a metal plate in order to have a unique temporal and spatial reference [see Fig. 6(a)]. This choice is useful because the metal totally reflects the signal passing through the sample allowing us to identify the time corresponding to summarized in Fig. 6(b). The samples are analyzed by collecting data on both sides (up and down) and with three different fibers orientations (see Fig. 7). In particular, the specimens are measured with the fibers oriented as shown in Fig. 7(a) (the starting position $\alpha = 0°$, where α is the angle between the fiber shown in red in Fig. 7 and the y-axis), rotated by $45°$ [$\alpha = 45°$, see Fig. 7(b)] and by $90°$ [$\alpha = 90°$, Fig. 7(c)], with respect to the initial position.

TABLE I
THICKNESS OF THE MAGS

Sample	$0A$	$1A$	$2A$	$3A$
$d_m\,[mm]$	1.55	1.40	1.50	1.30

Thickness of the magnetic scaffolds, d_m, measured with a manual gauge

The measurement protocol consists of six measures for each SuT and this is made because small variations in the results may occur, mainly due to two factors. The first one is the random placement of the sample on the scanning platform of the THz measurement system. The second one is the texture of the sample, which consists of 90°-interlaced fiber architecture, as described in Section II-B that can affect the propagation time of the THz signal within the object. The polymer matrix, as shown in Fig. 1, has empty spaces between the fibres, which alters the propagation of the THz signal. Furthermore, the time that the THz signal employs to propagate depends on the mutual position of the fibres, and thus, on their orientation with respect to the emitter and the receiver locations.

THz measurements were performed in uncontrolled environment conditions with temperature values in the range 28 °C–30 °C and humidity percentages from 30% to 35%. The data were gathered by scanning a 10 mm × 10 mm area with a 0.12 mm spatial offset along *x* and *y* axes, which was selected in agreement with the spatial variability of the geometrical features of the investigated samples. The time required to collect each dataset was less than 5 min, while the processing time was about a couple of minutes. Of course, such a time is not negligible but, in our opinion, is reasonable for high-precision laboratory measurements.

Moreover, the thickness of the samples in Fig. 2, say d_m, are shown in Table I. Such values were measured by means of a manual gauge, having an accuracy of about 10^{-1} mm.

IV. CHARACTERIZATION OF THE MAGS

This section is devoted to describe the approach to characterized the MagS, which can be summarized in the following steps:

1) estimation of the thickness (Δ);
2) estimation of the refractive index (η);
3) evaluation of the 2-D MNPs distribution map (MDM);
a) definition of THz propagation delay map (PDM);
b) definition of the magnetization index (I_m);
c) definition of THz reference propagation times (t_M, t_{NM});
d) definition of magnetization concentration mask (MCM);
e) definition of the magnetization distribution index (I_{md});

The approach is applied to the filtered THz data obtained as described in Section III-B. All THz data processing is done by using MATLAB codes.

A. Thickness Estimation

The thickness of the SuT (Δ, in mm), is computed by using the ToF formula, see (1). In particular, it is estimated as the difference between the distance from the emitter/receiver to the metallic surface on which the samples are placed, say d_1, and the distance between the emitter/receiver and the sample surface, i.e., the top of the scaffold, say d_2 (see Fig. 8). The distances d_1 and d_2 are computed according to the ToF formula (1)

$$d_i = \frac{c \cdot t_i}{2} \tag{2}$$

with $i = 1, 2$; where c is the speed of light in the vacuum (m/s) and t_i is the time, in ps that the waveform employs to propagate from the emitter to the metal plate (t_1) or to the top of the scaffold (t_2) and go back to the receiver.

The time t_1 has been estimated from the A-Scan obtained by averaging the collected waveforms referred to the parts of scanned area that are not covered by the scaffold and it is referred to as external area [see Fig. 9(a)]. This A-Scan takes into account the waveforms collected outside the sample, and t_1 is identified as the first minimum, calculated going back in time, starting from the peak of the reflected signal due to air-metal interface [see Fig. 9(b)].

The time t_2 is estimated from the A-Scan obtained by averaging the collected waveforms of the scanned area intercepting the scaffold, and referred to as internal area [see Fig. 9(a)]. In particular, t_2 is identified as the first minimum value, just before the peak due to air-sample interface [see Fig. 9(c)]. Once the two distances have been estimated, it is possible to estimate the thickness of the scaffold $\Delta = d_1 - d_2$.

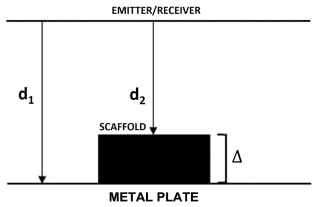

Fig. 8. d_1 is the distance between the emitter/receiver and the metal plate. d_2 is the distance between the emitter/receiver and the surface of the scaffold. Δ is the thickness of the object.

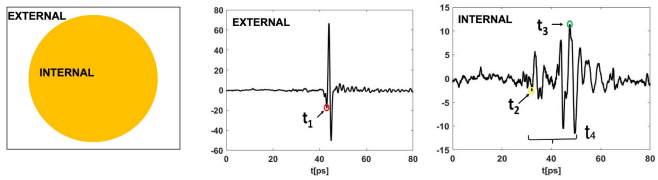

Fig. 9. (a) Scan Area: external and internal points exploited to derive the averaged A-scans. The yellow circle represents the scaffold. (b) Averaged A Scan from which the value of t_1, highlighted by a red circle, is derived. (c) Averaged A Scan used to derive the value of t_2 and t_3 pointed out by a yellow circle and a green one, respectively. t_4 represents the time that the waveform employs to propagate within the SuT.

B. Refractive Index Estimation

The second step involves the identification of the refractive index (η) of the analyzed samples and allows the characterization of the SuT from an EM point of view. Considering that MagS is

not homogeneous, the term refractive index denotes the effective refractive index. This value, once again, is derived from the ToF formula (1). Let v be the EM wave propagation velocity into the object, it is given by $v = \frac{c}{\eta}$. Hence, the refractive index η is derived as

$$\eta = \frac{c \cdot t_4}{2 \cdot \Delta} \tag{3}$$

where Δ is the estimated thickness of the object and t_4 represents the time that the waveform employs to propagate within the SuT. This time is given by the difference between the time instant t_3 corresponding to the peak of the reflected wave due to the object-metal interface and the time instant t_2 corresponding to the peak referred to top face of the scaffold [see Fig. 9(c)].

C. MNPs Spatial Distribution Estimation

To extract the spatial distribution of MNPs in the polymeric matrix, the THz PDM of the SuT is first derived. PDM is a 2-D image representing the propagation time delay of the THz wave due to the presence of MNPs into the scaffold. Such map is a 2-D differential image obtained by subtracting, for each pixel, the propagation time referred to the sample under test and a reference propagation time (t_{NM}) computed by considering an ideal homogeneous scaffold having the same thickness of the surveyed one but being without MNPs. The propagation time referred to the SuT is retrieved from the measured data, for each pixel of the scanned area intercepting the scaffold, as the value of the time interval occurring between the time instant of the peak due to the scaffold top face (air-scaffold interface), and the time instant of the peak due to the scaffold bottom face (scaffold-metal plate interface). Of course, the duration of this time range depends on the material wherein the signal propagation occurs and it is, therefore, affected by the presence and the amount of MNPs. The reference propagation time (t_{NM}) is the propagation time referred to a scaffold having the same thickness of the scaffold under test and the refractive index estimated for the sample 0 A in Fig. 2, i.e., the scaffold without MNPs. Then, the pixels of the scaffold wherein there are MNPs are detected from the PDM as the ones different from zero. The PDM allows the estimate of a magnetization index (I_m), synthetically encoding the amount of MNPs present in the SuT (with respect to a homogeneous reference). The I_m value is given by the ratio between the number of pixels containing MNPs and the total number of pixels discretizing the scanning area and intercepting the scaffold, i.e., the number P of pixels belonging to the internal area [see Fig. 9(a)]

$$I_m = \frac{\sum_{i,j=1}^{N,M}(x_{i,j} > 0)}{P} \tag{4}$$

being $x_{i,j}$ is the pixel considering and $N \times M$ is the dimension of the image.

Furthermore, the areas where the MNP are mainly concentrated are retrieved by introducing a threshold T defined by the difference between the times of flight of the reference scaffold without MNPs (t_{NM}) and the ToF for the one homogeneously loaded with MNPs (t_M). This latter is derived using the ToF formula [see (1)] where Δ is the thickness of the SuT and v is the EM wave velocity in an object having the refractive index η estimated for the SuT. The value T is used to threshold the PDM and to obtain a binary magnetization map, which is referred to as MCM. In this map, the pixels where the propagation time is larger than T are set to one, being estimated as the pixel where the presence of the MNPs significantly affects the THz signal propagation through the sample. The MCM allows the estimate of a magnetization distribution index (I_{md}), which accounts for the areas of the scaffolds where the MNPs are mostly concentrated (with respect to a homogeneous distribution of MNPs in the polymeric matrix). The I_{md} value has been calculated as the ratio between the number of pixels where the propagation time is larger than T and the total number of pixels P

$$I_{\text{md}} = \frac{\sum_{i,j=1}^{N,M}(x_{i,j} > T)}{P} \tag{5}$$

being $x_{i,j}$, N, and M defined as above.

Finally, the 2-D MNPs distribution map (MDM) is retrived by multiplying pixel by pixel the binary MCM and the map of the filtered THz signal amplitude (i.e., THz false colors image). This image is normalized to its maximum value and allows us to distinguish the areas of the SuT where MNPs are mostly concentrated and to detect how the distribution of the MNPs changes along x and y directions.

V. THz Results of the Case Studies

The results obtained for the MagS introduced in Section II-B (see Fig. 2) using the procedures detailed in Section IV are reported in this section.

Table II shows the time t_1, and the values t_2 and t_3, derived from the A-scans described in Section IV-A and IV-B, for the six measurement set up [see Fig. 6(b)]. These values were used to derive the thickness Δ and refractive index η shown in Table III, for measurement 1 to 6. In addition, for each sample the results of Δ and η were averaged:

1) M_{up} contains the average values of measurements 1–2–3 (i.e., sample upwards with three different fibre orientations: $\alpha = 0°, 90°, 45°$);
2) M_{down} contains the average of measurements 4–5–6 (i.e., sample downwards with three different fibre orientations: $\alpha = 0°, 90°, 45°$);
3) M_{tot} contains the average of all six measurements.

Table IV compares the average thickness values derived from THz data (Δ), referred to all the six measurements (M_{tot}), with those measured by means of a manual gauge (d_m), having an accuracy of about 10^{-1} mm. Table V shows at its first row the THz propagation times of the reference samples without MNPs (t_{NM}) exploited to derive the PDMs in Fig. 10, referring to the sample 1 A, 2 A, and 3 A.

The second row of Table V contains the instant times t_M referred to the scaffolds homogeneously loaded with MNPs that allow us to obtain the threshold T (see the third row of Table V) used to retrieve the MCMs shown in Figs. 11(b), 12(b), and

TABLE II
TIMES OF FLIGHT

	$t_1[ps]$				$t_2[ps]$				$t_3[ps]$			
Measurement	$0A$	$1A$	$2A$	$3A$	$0A$	$1A$	$2A$	$3A$	$0A$	$1A$	$2A$	$3A$
1	42.9	41.3	42.0	43.7	32.0	31.7	32.1	34.8	48.4	46.9	47.7	49.2
2	43.3	41.4	41.3	41.0	32.6	32.0	31.4	32.1	48.9	46.8	47.1	46.6
3	41.2	41.2	42.1	42.1	30.6	31.5	32.0	33.2	47.0	46.7	47.8	47.4
4	41.6	41.9	42.8	42.5	30.6	32.2	32.8	33.7	47.3	47.2	48.6	48.2
5	43.3	41.4	41.2	42.3	32.7	31.2	31.2	33.5	48.9	46.7	46.8	47.6
6	42.4	41.7	42.4	44.6	31.7	32.0	32.4	35.7	48.2	47.0	48.5	49.8

t_1, t_2 and t_3 in ps for all the measurement set.

TABLE III
ESTIMATED THICKNESS AND REFRACTIVE INDEX OF THE SUT.

	$0A$ **[mm]**		$1A$		$2A$		$3A$	
Measurement	Δ[mm]	η	Δ[mm]	η	Δ[mm]	η	Δ[mm]	η
1	1.62	1.52	1.47	1.56	1.50	1.56	1.34	1.61
2	1.61	1.52	1.41	1.57	1.50	1.58	1.34	1.61
3	1.59	1.54	1.45	1.57	1.50	1.58	1.33	1.60
4	1.65	1.52	1.45	1.55	1.49	1.59	1.32	1.65
5	1.58	1.54	1.45	1.55	1.50	1.57	1.32	1.60
6	1.60	1.55	1.45	1.55	1.51	1.60	1.34	1.58
M_{up}	1.61	1.53	1.44	1.57	1.50	1.57	1.34	1.61
M_{down}	1.61	1.54	1.45	1.55	1.50	1.59	1.33	1.61
M_{tot}	1.61	1.53	1.45	1.56	1.50	1.58	1.33	1.61

Δ and η values for each measurement and their averages M_{up}, M_{down}, M_{tot}.

TABLE IV
MEASURED THICKNESS AND ESTIMATED AVERAGED THICKNESS.

Sample	$0A$	$1A$	$2A$	$3A$
$d_m[mm]$	1.55	1.40	1.50	1.30
$\Delta[mm]$	1.61	1.45	1.50	1.33

Thickness of the magnetic scaffolds: d_m is the value measured with a manual gauge - Δ is the averaged thickness estimated for all the measurement set.

TABLE V
TOF OF THE REFERENCE SCAFFOLD WITHOUT MNP; TOF OF THE REFERENCE SCAFFOLD HOMOGENEOUSLY LOADED WITH MNP; THRESHOLDS

Sample	$1A$	$2A$	$3A$
$t_{NM}[ps]$	14.70	15.30	13.56
$t_M[ps]$	15.00	15.80	14.28
$T[ps]$	0.30	0.50	0.72

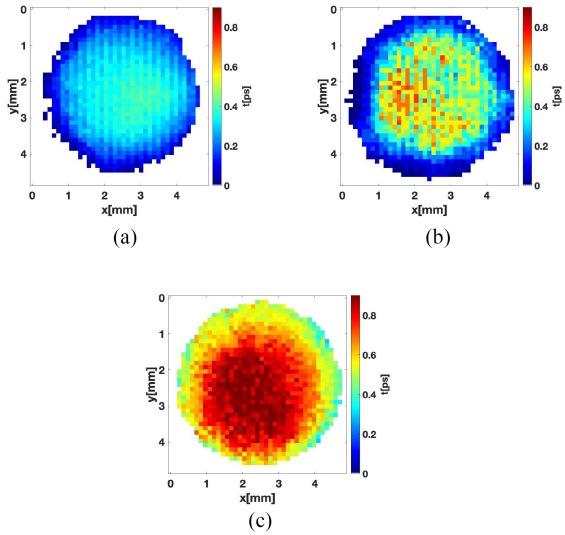

(a) (b) (c)

Fig. 10. PDM. (a) 1 A. (b) 2 A. (c) 3 A.

TABLE VI
MAGNETIZATION INDEX AND MAGNETIZATION DISTRIBUTION INDEX

Sample	$0A$	$1A$	$2A$	$3A$
I_m	0	0.88	0.97	0.99
I_{md}	0	0.14	0.27	0.48

I_m and I_{md} for the MagS.

13(b). Table VI contains the magnetization index (I_m) and the magnetization distribution index (I_{md}).

The 2-D MDM are in Figs. 11(c), 12(c), and 13(c), where the optical image of the corresponding MagS is also shown.

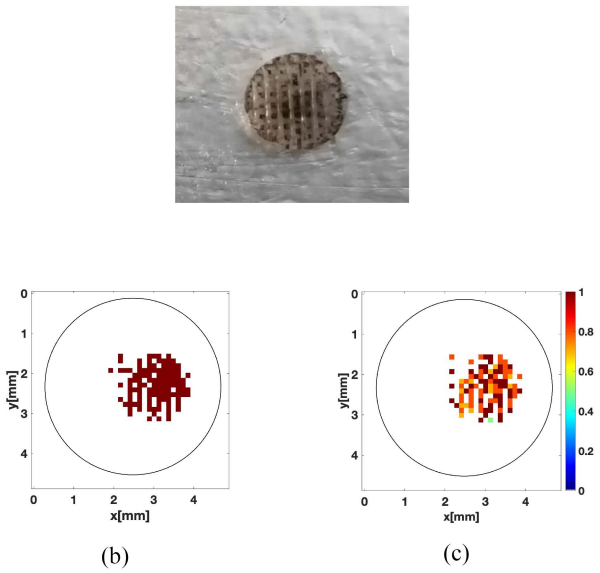

Fig. 11. (a) Photograph of the MagS 1 A. (b) MCM 1 A. (c) 2-D MDM 1 A.

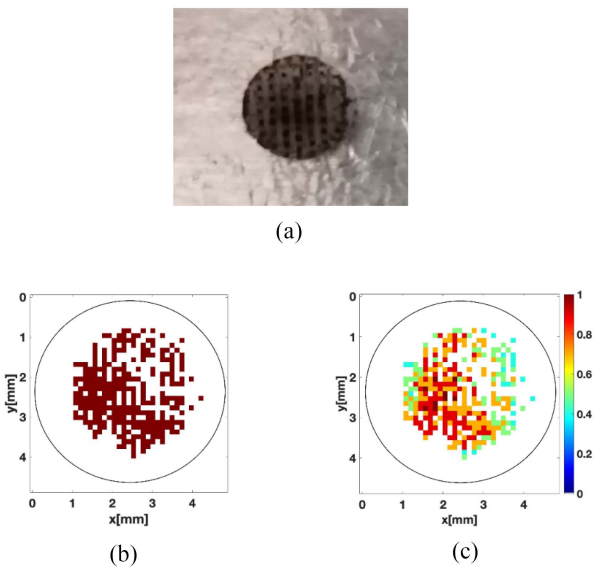

Fig. 12. (a) Photograph of the MagS 2 A. (b) MCM 2 A. (c) 2-D MDM 2 A.

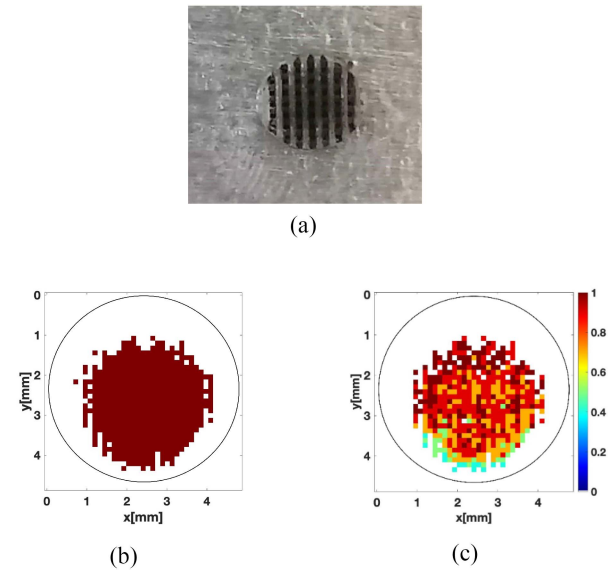

Fig. 13. (a) Photograph of the MagS 3 A. (b) MCM 3 A. (c) 2-D MDM 3 A.

VI. Discussion

THz data referred to the six measurement setups shown in Table II have been used to estimate Δ and η, and the results are presented in Table III.

As shown in Table III, small variations in the results occur due to the different position of the MagS texture, which is made by 90°-shifted highly porous mesh, on the scanning platform of the THz system. The texture of the MagS and the presence of empty spaces between fibers affect the ToF, which depends on the mutual position of the fibers and on their orientation with respect to the emitter and the receiver.

There are also small variations in the results of Δ and η, as shown from the row 1 to 6 in Table III, due to the fact that such values are computed from the instant times t_1, t_2, and t_3 (see Sections IV-A and IV-B).

Table III shows the estimated values of Δ and η for the single measure (from rows 1 to 6) and for the averaged measures. The results do not differ significantly each other if we consider an approximation to the first digit. Therefore, they suggest that a single measurement could be sufficient, even if the average of three measurements, with the sample up or down, or six measurements (i.e., MagS up and down) increases the robustness of the MagS characterization.

The effectiveness of the procedures described in Section IV-A is demonstrated by comparing the averaged values estimated from THz data Δ (i.e., referred to M_{tot}), and the values measured by the manual gauge d_m having accuracy of about 10^{-1} mm. Table IV demonstrates that the proposed method gives good results considering the accuracy of the manual gauge. It is worth noting that, as shown in Table III, the sample without MNPs (i.e., 0 A) has the lowest η value, as expected, while the other samples show an increasing trend. In particular, sample 3 A is characterized by the highest η value and this is compliant with the largest amount of MNPs.

The PDMs shown in Fig. 10 contain the THz propagation delay, in ps, introduced by the presence of MNP and allow the introduction of the magnetization indices, I_m, shown in the first row of Table VI. The obtained results state, as foreseeable, that when the amount of MNP increases also η increases, while I_m approaches to 1. Moreover, the results referred to I_{md} (see second row of Table VI) show that higher I_{md} values correspond to larger areas where MNPs are concentrated, which is confirmed by both the MCM and the picture of the MagS.

Looking at the photo of sample 1 A in Fig. 11(a), it is possible to note that there is a higher MNP concentration in the center, as confirmed by the MCM in Fig. 11(b). Similarly, for the sample 2 A, the MNPs are present in lower amounts at the edges, while

they are present in higher amounts in the other parts of the scaffolds, as shown in the photo of the specimen in Fig. 12(a) and confirmed by the MCM [see Fig. 12(b)]. Finally, sample 3 A appears to have a higher MNP concentration, as confirmed by the photography in Fig. 13(a) as well as by our results in Fig. 13(b).

The 2-D maps of MNP distribution in Figs. 11(c), 12(c), and 13(c), each normalized to its maximum value, allow us to see how the MNP distribution changes along x- and y-axis in the areas where they are present in greater amounts. Fig. 11(c) shows that MNP are distributed almost homogeneously in the sample 1 A, but they are in a limited part of the scaffold. Conversely, Fig. 12(c), referring to the sample 2 A, shows a larger presence of MNPs in the central region (x ranging from 1.5 to 3 mm and y between 1 and 3.5 mm). Sample 3 A [see Fig. 13(c)], which contains the largest amount of MNPs, has a homogeneous distribution along the x and y axes like sample 1 A, and in this case MNP fill almost the entire scaffold.

VII. Conclusion

This article has proposed a strategy exploiting THz technology for nondestructive inspection of composite materials, especially MagS, which are used in various biomedical applications.

The presented approach allows a quantitative characterization providing an estimate of the thickness (Δ) and refractive index (η) of the MagS. In addition, two reference propagation time are introduced. The procedure allows us to define two indices, the magnetization index, I_m, and the magnetization distribution index, I_{md}, which take into account the areas where MNPs occur and give us information about the region where they are present in greater quantities, respectively.

It is worth noting that THz imaging enables nondestructive characterization without the use of ionizing radiation, as in MicroCTs, and with a less complex and laborious measurement procedure (i.e., the samples are simply placed on the scanning area of the THz system) compared to other techniques, such as SEM and TEM. Furthermore, unlike other nondestructive techniques, THz ToF imaging has the advantage of allowing a 3-D characterization of the object under test.

To the best of authors' knowledge, this article presents a novel method based on the use of THz nondestructive characterization of MagS used for biomedical applications. The proposed approach and the results could be relevant to materials scientists, bioengineers, and clinicians who want to fabricate, characterize, and use MagS as multifunctional tools for tissue engineering, drug delivery, and hyperthermia. The results presented in this article support the possibility of using THz technology to improve MagS fabrication techniques. Moreover, they open new challenges aimed at 3-D characterization of the MagS (i.e., evaluation of the volumetric distribution of the MNPs in the scaffold), which would allow estimation of the concentration of the MNPs in the polymer matrix.

References

[1] M. M. Schwartz, "Composite Materials Handbook". Warrendale, PA, USA: SAE International,1983.

[2] K. P. Mallick, *Composites Engineering Handbook*, Boca Raton, FL, USA: CRC Press, 1997.

[3] R. M. Jones, *Mechanics of Composite Materials*. New York, NY, USA: Taylor & Francis, 1999.

[4] A. E. Bogdanovich and R. L. Sierakowski, "Composite materials and structures: Science, technology and applications—A compendium of books, review papers, and other sources of information," *Appl. Mech. Rev.*, vol. 52, pp. 351–366, 1999.

[5] I. F. A. Lopez and A. Mendikute, "In introductory review to THz nondestructive testing of composite mater," *J. Infrared, Millimeter, Terahertz Waves*, vol. 34, no. 2, pp. 152–169, 2013.

[6] V. M. Antonucci et al., "Resin flow monitoring in resin film infusion process," *J. Mater. Process. Technol.*, vol. 143, pp. 687–692, 2003.

[7] S. Bickerton, E. M. P. S. Šimácek, and S. G. Advani, "Fabric structure and mold curvature effects on preform permeability and mold filling in the RTM process. Part II. Predictions and comparisons with experiments," *Composites Part A: Appl. Sci. Manuf.*, vol. 31, no. 5, pp. 439–458, 2000.

[8] B. Qi, J. Raju, T. Kruckenberg, and R. Stanning, "A resin film infusion process for manufacture of advanced composite structures," *Composite Struct.*, vol. 47, no. 1–4, pp. 471–476, 1999.

[9] P. IP Soares et al., Design and engineering of magneto-responsive devices for cancer theranostics: Nano to macro perspective, *Materials Sci.*, 116, 2021, Art. no. 100742.

[10] O. Sedighi, A. Alaghmandfard, M. Montazerian, and F. Baino, "A critical review of bioceramics for magnetic hyperthermia," *J. Amer. Ceram. Soc.*, vol. 105, no. 3, pp. 1723–1747, 2022.

[11] M. B. Lodi, A. Fanti, A. Vargiu, M. Bozzi, and G. Mazzarella, "A multiphysics model for bone repair using magnetic scaffolds for targeted drug delivery," *IEEE J. Multiscale Multiphys. Comput. Tech.*, vol. 6, pp. 201–213, Dec. 2021.

[12] S. Behrens, "Preparation of functional magnetic nanocomposites and hybrid materials: Recent progress and future directions," *Nanoscale*, vol. 3, no. 3, pp. 877–892, 2011.

[13] S. Sprio et al., "A graded multifunctional hybrid scaffold with superparamagnetic ability for periodontal regeneration," *Int. J. Mol. Sci.*, vol. 19, no. 11, pp. 3604, 2018.

[14] Y. Li et al., "Magnetic hydrogels and their potential biomedical applications," *Adv. Funct. Mater.*, vol. 23, no. 6, pp. 660–672, 2013.

[15] S. Li, C. Wei, and Y. Lv, "Preparation and application of magnetic responsive materials in bone tissue engineering," *Curr. Stem Cell Res. Ther.*, vol. 15, no. 5, pp. 428–440, 2020.

[16] A. Russo et al., "Bone regeneration in a rabbit critical femoral defect by means of magnetic hydroxyapatite macroporous scaffolds," *J. Biomed. Mater. Res. Part B: Appl. Biomaterials*, vol. 106, no. 2, pp. 546–554, 2018.

[17] J. Huang et al., "Preparation and biocompatibility of diphasic magnetic nanocomposite scaffold," *Mater. Sci. Engineering: C*, vol. 87, pp. 70–77, 2018.

[18] Y. Zhao et al., "Magnetic bioinspired micro/nanostructured composite scaffold for bone regeneration," *Colloids Surfaces B: Biointerfaces*, vol. 174, pp. 70–79, 2019.

[19] M. B. Lodi, A. Fanti, G. Muntoni, and G. Mazzarella, "A multiphysic model for the hyperthermia treatment of residual osteosarcoma cells in upper limbs using magnetic scaffolds," *IEEE J. Multiscale Multiphys. Comput. Tech.*, vol. 4, pp. 337–347, Dec. 2019.

[20] R. D. Santis et al., "A basic approach toward the development of nanocomposite magnetic scaffolds for advanced bone tissue engineering," *J. Appl. Polym. Sci.*, vol. 122, no. 6, pp. 3599–3605, 2011.

[21] M. Bañobre-López et al., "Poly (caprolactone) based magnetic scaffolds for bone tissue engineering," *J. Appl. Phys.*, vol. 109, no. 7, 2011, Art. no. 07B313.

[22] J.-J. Kim et al., "Magnetic scaffolds of polycaprolactone with functionalized magnetite nanoparticles: Physicochemical, mechanical, and biological properties effective for bone regeneration," *Rsc Adv.*, vol. 4, no. 33, pp. 17325–17336, 2014.

[23] A. Hajinasab, S. Saber-Samandari, S. Ahmadi, and K. Alamara, "Preparation and characterization of a biocompatible magnetic scaffold for biomedical engineering," *Mater. Chem. Phys.*, vol. 204, pp. 378–387, 2018.

[24] A. C. Small and J. H. Johnston, "Novel hybrid materials of magnetic nanoparticles and cellulose fibers," *J. Colloid Interface Sci.*, vol. 331, no. 1, pp. 122–126, 2009.

[25] H.-M. Yun et al., "Magnetic nanocomposite scaffolds combined with static magnetic field in the stimulation of osteoblastic differentiation and bone formation," *Biomaterials*, vol. 85, pp. 88–98, 2016.

[26] H. Skaat et al., "Magnetic scaffolds enriched with bioactive nanoparticles for tissue engineering," *Adv. Healthcare Mater.*, vol. 1, no. 2, pp. 168–171, 2012.
[27] C. Gervais, M. Thoury, S. Réguer, P. Gueriau, and J. Mass, "Radiation damages during synchrotron x-ray micro-analyses of prussian blue and zinc white historic paintings: Detection, mitigation and integration," *Appl. Phys. A*, vol. 121, no. 3, pp. 949–955, 2015.
[28] P. R. Sivakumar, A. Ramesh, S. R. Ponnusamy, and C. Muthamizhchelvan, "Synthesis and characterization of nickel ferrite magnetic nanoparticles," *Mater. Res. Bull.*, vol. 46, no. 12, pp. 2208–2211, 2011.
[29] V. Barge, P. Yendhe, K. Kodre, S. Attarde, and R. Patil, "Electron microscopy: A review," *World J. Pharmaceutical Res.*, vol. 3, no. 4, pp. 313–333, 2014.
[30] A. Priya, A. Singh, and N. A. Srivastava, "Electron microscopy—An overview," *Int. J. Students' Res. Technol. Manage.*, vol. 5, no. 4, pp. 81–87, 2017.
[31] S. Wietzke et al., "Terahertz spectroscopy on polymers: A review of morphological studies," *J. Mol. Struct.*, vol. 1006, no. 1–3, pp. 41–51, 2011.
[32] Z. D. Taylor et al., "THz medical imaging: In vivo hydration sensing," *IEEE Trans. Science. Technol.*, vol. 1, no. 1, pp. 201–219, Sep. 2011.
[33] K. Ajito, "Terahertz spectroscopy for pharmaceutical and biomedical applications," *IEEE Trans. THz Sci. Technol.*, vol. 5, no. 6, pp. 1140–1145, Nov. 2015.
[34] R. Knipper et al., "THz absorption in fabric and its impact on body scanning for security application," *IEEE Trans. THz Sci. Technol.*, vol. 5, no. 6, pp. 999–1004, Nov. 2015.
[35] I. Catapano and F. Soldovieri, "A data processing chain for terahertz imaging and its use in artwork diagnostics," *J. Infrared, Millimeter, Terahertz Waves*, vol. 38, no. 4, pp. 518–530, 2017.
[36] S. Zappia, L. Crocco, and I. Catapano, "THz imaging for food inspections: A technology review and future trends," *Terahertz Technol.*, pp. 91–106, 2021.
[37] E. V. Yakovlev, K. I. Zaytsev, I. N. Dolganova, and S. O. Yurchenko, "Nondestructive evaluation of polymer composite materials at the manufacturing stage using terahertz pulsed spectroscopy," *IEEE Trans. Terahertz Sci. Technol.*, vol. 5, no. 5, pp. 810–816, Sep. 2015.
[38] Y.-S. Lee, *Principles of Terahertz Science and Technology*, vol. 170. New York, NY, USA: Springer, 2009.
[39] J. A. Hejase, P. R. Paladhi, and P. P. Chahal, "Terahertz characterization of dielectric substrates for component design and nondestructive evaluation of packages," *IEEE Trans. Compon. Packag. Manuf. Technol.*, vol. 1, no. 11, pp. 1685–1694, Nov. 2011.
[40] L. Cheng and G. Y. Tian, "Comparison of nondestructive testing methods on detection of delaminations in composites," *J. Sensors*, vol. 2012, pp. 1–7, 2012.
[41] R. Bogue, "New NDT techniques for new materials and applications," *Assem. Autom.*, vol. 32, no. 3, pp. 211–215, 2012.
[42] P. Lopato and T. Chady, "Time reversal pulsed terahertz inspection of dielectric structures," *Int. J. Appl. Electromagnetics Mech.*, vol. 39, no. 1–4, pp. 427–433, 2012.
[43] D. K. Hsu, K.-S. Lee, J.-W. Park, Y.-D. Woo, and K.-H. Im, "NDE inspection of terahertz waves in wind turbine composites," *Int. J. Precis. Eng. Manuf.*, vol. 13, no. 7, pp. 1183–1189, 2012.
[44] F. Ospald et al., "Aeronautics composite material inspection with a terahertz time-domain spectroscopy system," *Opt. Eng.*, vol. 53, no. 3, 2013, Art. no. 031208.
[45] E. Cristofani et al., "Nondestructive testing potential evaluation of a terahertz frequency-modulated continuous-wave imager for composite materials inspection," *Opt. Eng.*, vol. 53, no. 3, 2014, Art. no. 031211.
[46] B. M. Fischer et al., "Investigating material characteristics and morphology of polymers using terahertz technologies," *IEEE Trans. THz Sci. Technol.*, vol. 3, no. 3, pp. 259–268, May 2013.
[47] M. L. Mather et al., "Image-based characterization of foamed polymeric tissue scaffolds," *Biomed. Mater.*, vol. 3, no. 1, 2008, Art. no. 015011.
[48] F. Rutz et al., "Terahertz quality control of polymeric products," *Int. J. Infrared Millimeter Waves*, vol. 27, no. 4, pp. 547–556, 2006.
[49] S. C. Wietzke et al., "Industrial applications of THz systems," in *Proc. Int. Symp. Photoelectronic Detection Imag. Terahertz High Energy Radiat. Detection Technol. Appl. Int. Soc. Opt. Photon.*, 2009, vol. 7385, Art. no. 738506.
[50] F. Destic and C. Bouvet, "Impact damages detection on composite materials by THz imaging," *Case Stud. Nondestruct. Testing Eval.*, vol. 6, pp. 53–62, 2016.
[51] V. Egor et al., "Nondestructive testing of polymer composite materials using THz radiation," in *Proc. J. Phys.: Conf. Ser.*, 2014, vol. 486, Art. no. 0 12008.
[52] M. B. Lodi et al., "Influence of magnetic scaffold loading patterns on their hyperthermic potential against bone tumors," *IEEE Trans. Bio-Medical Eng.*, vol. 69, no. 6, pp. 2029–2040, Jun. 2022.
[53] S I. Zappia et al., "Magnetic nanoparticles distribution estimate in polymeric scaffolds using THz imaging," in *Proc. 24th Nat. Meeting Electromagnetics (Rinem 2022)*, 2022.
[54] S L. Zappia et al., "Terahertz imaging of magnetic scaffolds," in *Proc. 6th Nat. Conf. Interaction Electromagn. Fields Biosyst.* 2022.
[55] B. Dhandayuthapani, Y. Yoshida, T. Maekawa, and D. Sakthi Kumar, "Polymeric scaffolds in tissue engineering application: A review," *Int. J. Polym. Sci.*, vol. 2011, pp. 1–19 2011.
[56] L. E. Freed and G. Vunjak-Novakovic, "Culture of organized cell communities," *Adv. Drug Del. Rev.*, vol. 33, no. 1/2, pp. 15–30, 1998.
[57] V. Karageorgiou and D. Kaplan, "Porosity of 3 d biomaterial scaffolds and osteogenesis," *Biomaterials*, vol. 26, no. 27, pp. 5474–5491, 2005.
[58] J. Takayanagi et al., "High-resolution time-of-flight terahertz tomography using a femtosecond fiber laser," *Opt. Exp.*, vol. 17, no. 9, pp. 7533–7539, 2009.
[59] D. M. Mittleman, R. H. Jacobsen, and M. C. Nuss, "T-ray imaging," *IEEE J. Sel. Topics Quantum Electron.*, vol. 2, no. 3, pp. 679–692, Sep. 1996.
[60] I. Catapano, A. Affinito, L. Guerriero, B. Bisceglia, and F. Soldovieri, "Majolica imaging with THz waves: Preliminary results," *Appl. Phys. A*, vol. 122, no. 5, pp. 533, 2016.
[61] W. Köhler et al., "Non-destructive investigation of paintings with THz-radiation," *Eur. Conf. Non-Destruct.*, Testing. No. P181, 2006.
[62] K. Konstantinides, B. Natarajan, and G. S. Yovanof, "Noise estimation and filtering using block-based singular value decomposition," *IEEE Trans. Image Process.*, vol. 6, no. 3, pp. 479–483, Mar. 1997.

Sonia Zappia received the master's degree in biomedical engineering in 2019 from "Federico II" University of Naples, Naples, Italy, where she is currently working toward the Ph.D. degree with the Department of Electrical Engineering and Information Technology. Her Ph.D. studies aim to explore the potential of THz imaging in the field of food and biomedical industries performing controlled experiments and developing processing techniques to enhance THz capabilities in non destructive inspection (NDI) and material characterization.

In 2019, she was with the Regional Center Information Communication Technology (CeRICT), Naples, Italy. Since 2020, she has been with the Institute of Electromagnetic Sensing of the Environment, National Research Council of Italy (IREA-CNR), Naples, Italy, as a Research Fellow. Her research activity involves imaging with terahertz (THz) time-domain signals and THz spectroscopy.

Rosa Scapaticci (Member, IEEE) received the M.S. Laurea degree (*summa cum laude*) in biomedical engineering from "Federico II" University of Naples, Naples, Italy, in 2010 and the Ph.D. degree in information engineering from the "Mediterranea" University of Reggio Calabria, Reggio Calabria, Italy, in 2014.

Since December 2013, she has been with the Institute of Electromagnetic Sensing of the Environment, National Research Council of Italy (IREA-CNR), Naples, Italy, first as a Research Fellow and since September 2017 as a Researcher. He has coauthored more than 90 papers on international journals and conference proceedings. Her scientific interests include electromagnetic scattering problems, imaging methods for noninvasive diagnostics and they are mainly focused on the development of innovative microwave imaging approaches in the framework of biomedical applications, as well as therapeutic applications of electromagnetic fields.

Dr. Scapaticci was the recipient of the best Student Member Paper Award from the IEEE Antennas and Propagation Society Central and Southern Italy Chapter, in 2013 and the Italian Society of Electromagnetics, the Barzilai Award and the Latmiral Award in September 2014 and in September 2018, respectively.

Matteo Bruno Lodi (Member, IEEE) received the bachelor's degree in biomedical engineering from the University of Cagliari, Cagliari, Italy, in 2016, the master's degree in biomedical engineering from Politecnico di Torino, Turin, Italy, in 2018, and the Ph.D. (Hons.) degree in electronic engineering and computer science from the University of Cagliari in 2022.

He is currently a Technologist with the Applied Electromagnetics Group, University of Cagliari. His research interests include the modeling of bioelectromagnetic phenomena, especially hyperthermia treatment; the study, manufacturing, and synthesis of magnetic biomaterials for tissue engineering applications; and the use of microwaves for biotechnology and environmental applications, while working in the design and characterization of antennas for space and wearable applications.

Dr. Lodi has been awarded as Young Scientists at the General Assembly and Scientific Symposium of URSI in 2020 and 2021. He was the recipient of the Best Poster Award at IX International School of Bioelectromagnetism "Alessandro Chiabrera" in 2019. In 2021, he was a coauthor of the "2021 IEEE IST Best Student Paper Award" at IEEE International Conference on Imaging Systems and Techniques.

Alessandro Fanti (Senior Member, IEEE) received the Laurea degree in electronic engineering and the Ph.D. degree in electronic engineering and computer science from the University of Cagliari, Cagliari, Italy, in 2006 and 2012, respectively.

From 2013 to 2016, he was a Postdoctoral Fellow of the Electromagnetic Group, University of Cagliari, where he is currently an Assistant Professor. He has authored or coauthored 57 papers in international journals. His research interests include the use of numerical techniques for modes computation of guiding structures, optimization techniques, analysis and design of waveguide slot arrays, analysis and design of patch antennas, radio propagation in urban environment, modeling of bioelectromagnetic phenomena, and microwave exposure systems for biotechnology and bioagriculture.

Giuseppe Ruello (Senior Member, IEEE) was born in Naples, Italy, in 1975. He received the Laurea degree (*cum laude*) in telecommunication engineering and the Ph.D. degree in information engineering from the University of Naples Federico II, Naples, Italy, in 1999 and 2003, respectively.

In 2002 and from 2004 to 2005, he was a Visiting Scientist with the Department of Signal Theory and Communications, Universitat Politecnica de Catalunya, Barcelona, Spain. He is currently a tenure-track Assistant Professor of Electromagnetics with the Department of Electrical Engineering and Information Technology, University of Naples Federico II. His research interests include synthetic aperture radar (SAR) remote sensing, modeling of electromagnetic scattering from natural surfaces, fractal models, SAR raw signal simulation, modeling of electromagnetic field propagation in urban environment, and remote sensing techniques for low-income semiarid regions.

Lorenzo Crocco (Senior Member, IEEE) received the Laurea degree (summa cum laude) in electronic engineering and the Ph.D. degree in applied electromagnetics from the University of Naples "Federico II," Naples, Italy, in 1995 and 2000, respectively.

He is currently a Research Director with the Institute for the Electromagnetic Sensing of the Environment, National Research Council of Italy (IREA-CNR), Naples. In 2001, he joined IREA-CNR. He has authored or coauthored more than 120 papers, given keynote talks and lectures, and led or participated to national and international research projects in the areas of his research fields. His scientific activities mainly concern electromagnetic scattering, with a focus on diagnostic and therapeutic uses of EM fields, noninvasive electromagnetic inspections, through-the-wall radar, and GPR.

Dr. Crocco is an Associate Editor for IEEE JOURNAL OF ELECTROMAGNETICS, RF AND MICROWAVES IN MEDICINE AND BIOLOGY (IEEE J-ERM) and has edited a book on electromagnetic technologies for brain diseases diagnostics, monitoring, and therapy. He has been an Italian representative in the Management Committees of COST actions devoted to medical applications of EM fields (MiMed on microwave imaging and MyWAVE on therapeutic applications of electromagnetic waves). Since 2015, he has been Member of the Board for the European School of Antennas (ESOA). Since 2017, he has been a Member of the Board of Directors of the Italian Electromagnetic Society (SIEm). He was the recipient of the Full Professor Habilitation in electromagnetic fields, by the Italian Ministry of Research and University, in 2018, SIEm "Barzilai" Award for Young Scientists (2004), and YSA at the URSI General Assembly held in New Delhi (India) in 2005. Since 2019, he has been a Member of the Italian URSI Commission (International Union of Radio Science). In 2019, he has been elected in the Scientific Board of the Engineering Department (DIITET) of CNR. He is a Fellow of the Electromagnetic Academy (TEA) and a URSI Senior Member.

Ilaria Catapano (Member, IEEE) received the Ph.D. degree in electric and information engineering from the University of Cassino, Cassino, Italy, in 2006.

In 2003, in the framework of her Ph.D. project, she started her research activity with the Institute for Electromagnetic Sensing of the Environment, National Research Council of Italy (IREA-CNR), Naples, Italy, where she is a Senior Researcher. He has coauthored more than 150 articles, mainly in scientific journals or proceedings of international conferences. Her research activities deal with noninvasive electromagnetic diagnostics and are mainly focused on models and strategies for electromagnetic forward and inverse scattering problems, development and performance assessment of microwave imaging approaches for shape reconstruction, processing of experimental data gathered by radar systems for subsurface surveys, and THz spectroscopy and imaging.

Dr. Catapano was the recipient of the G. Barzilai Award from the Italian Electromagnetic Society in 2004; she was one of the young scientist awardees at the 29th URSI General Assembly in 2008.